

The High Efficiency of Photosystem I in the Green Alga *Chlamydomonas reinhardtii* Is Maintained after the Antenna Size Is Substantially Increased by the Association of Light-harvesting Complexes II*[§]

Received for publication, August 27, 2015, and in revised form, October 11, 2015. Published, JBC Papers in Press, October 26, 2015, DOI 10.1074/jbc.M115.687970

Clotilde Le Quiniou, Bart van Oort, Bartłomiej Drop, Ivo H. M. van Stokkum, and Roberta Croce¹

From the Department of Physics and Astronomy, Faculty of Sciences, VU University Amsterdam and Institute for Lasers, Life and Biophotonics Amsterdam, LaserLaB Amsterdam, De Boelelaan 1081, 1081 HV Amsterdam, The Netherlands

Background: Photosystems acclimate to different light conditions modulating their antenna size.

Results: In PSI-LHCI-LHCII, energy transfer from LHCII to Photosystem I is relatively slow but still very efficient.

Conclusion: The association of LHCII to PSI increases its absorption cross section by ~50%, maintaining ~96% quantum efficiency.

Significance: The antenna size of PSI can be increased considerably without sacrificing its efficiency.

Photosystems (PS) I and II activities depend on their light-harvesting capacity and trapping efficiency, which vary in different environmental conditions. For optimal functioning, these activities need to be balanced. This is achieved by redistribution of excitation energy between the two photosystems via the association and disassociation of light-harvesting complexes (LHC) II, in a process known as state transitions. Here we study the effect of LHCII binding to PSI on its absorption properties and trapping efficiency by comparing time-resolved fluorescence kinetics of PSI-LHCI and PSI-LHCI-LHCII complexes of *Chlamydomonas reinhardtii*. PSI-LHCI-LHCII of *C. reinhardtii* is the largest PSI supercomplex isolated so far and contains seven Lhcbs, in addition to the PSI core and the nine Lhcas that compose PSI-LHCI, together binding ~320 chlorophylls. The average decay time for PSI-LHCI-LHCII is ~65 ps upon 400 nm excitation (15 ps slower than PSI-LHCI) and ~78 ps upon 475 nm excitation (27 ps slower). The transfer of excitation energy from LHCII to PSI-LHCI occurs in ~60 ps. This relatively slow transfer, as compared with that from LHCI to the PSI core, suggests loose connectivity between LHCII and PSI-LHCI. Despite the relatively slow transfer, the overall decay time of PSI-LHCI-LHCII remains fast enough to assure a 96% trapping efficiency, which is only 1.4% lower than that of PSI-LHCI, concomitant with an increase of the absorption cross section of 47%. This indicates that, at variance with PSII, the design of PSI allows for a large increase of its light-harvesting capacities.

In eukaryotic organisms, the photosynthetic apparatus contains two main pigment-protein complexes, embedded in the thylakoid membrane, Photosystems (PS)² I and II, that harvest light energy and convert it into chemical energy (1). The PS performances are largely determined by their capacities to harvest light and transfer excitation energy to the reaction center (RC) where charge separation occurs (2). To efficiently harvest light, PSI and PSII are equipped with two types of antennae. The inner antenna is composed of chlorophyll (Chl) *a*-binding complexes that together with the RC form the core complex. The core complexes of PSI and PSII bind 98 and 35 Chls, respectively (3, 4) and are highly conserved in eukaryotic organisms (5). The outer antenna, by contrast, varies in the different organisms as it is optimized for the absorption in their light-growth conditions (2). In plants and green algae, it is composed of members of the light-harvesting complex (Lhc) multigenic family, each coordinating between 10 and 14 Chls (*a* and *b*) (6, 7).

Despite the high sequence similarity, the number and properties of the Lhcs vary in plants and algae. LHCII trimers are composed of three major Lhcbs in *Arabidopsis thaliana* (Lhcb1–3 (8)) and of nine major Lhcbs in the green alga *Chlamydomonas reinhardtii*. (LhcbM1–9 (9)). Three monomeric antenna, CP29 (Lhcb4), CP26 (Lhcb5), and CP24 (Lhcb6), located between the core and the LHCII trimers, are present in *A. thaliana* PSII-LHCII (10), whereas CP24 is absent in *C. reinhardtii*, resulting in a different organization of the PSII-LHCII supercomplex in the two organisms (11, 12). Concerning PSI-LHCI, in *A. thaliana*, four Lhcas (Lhca1–4) are associated with the PSI core (13), forming a PSI-LHCI complex that contains 155 Chls (14, 15). In *C. reinhardtii*, nine Lhcas compose the antenna of PSI (16), which is far larger than that of plants (17, 18).

* This work was supported by the European Research Council (ERC) Consolidator Grant 281341 (ASAP) (to R. C.) and by the Netherlands Organization for Scientific Research (NWO) through a Vici grant (to R. C.) and a Veni grant (to B. v. O.). The authors declare that they have no conflicts of interest with the contents of this article.

§ This article contains S11: Materials and Methods, S12: Results from the target analysis, and S13: Quantifying the contributions of compartment size, composition and connectivity to the average decay time of PSI-LHCI and PSI-LHCI-LHCII.

¹ To whom correspondence should be addressed. Tel: 31-20-5986310; E-mail: r.croce@vu.nl.

² The abbreviations used are: PS, Photosystem; LHC, light-harvesting complex; RC, reaction center; Chl, chlorophyll; DAS, decay-associated spectra; SAS, species-associated spectra.

Excitation Energy Transfer in PSI-LHCI-LHCII of *C. reinhardtii*

The amount of excitation energy delivered to the RCs by the Lhcs does not only depend on their number but also on their biochemical and spectroscopic properties (19). The different affinity for Chl *a* and *b* between Lhcas and Lhcb and the presence of far-red absorbing forms in Lhcas (20, 21) results in differences in the wavelength-dependent light-harvesting capacities of the two photosystems. This creates an excitation imbalance that can affect electron transport and induce photo-damage (22). To avoid this and maintain a maximal photosynthetic efficiency, plants and algae regulate the association of Lhcb with PSI and PSII in a process known as state transitions (23, 24), in which mobile LHCII is associated with PSII in state 1 and with PSI in state 2. In plants, the mobile LHCII represents ~15% of the total LHCII population, and under sunlight, it is mainly associated with PSI *i.e.* plants in light are in state 2 (25).

The mechanisms of state transitions in the green alga *C. reinhardtii* seem to differ from what is observed in plants (26–28). For a long time, this difference was believed to be the pool size of LHCII involved in the transitions (80% according to Ref. 29); however, recent results suggest that the mechanism and probably also the physiological role of this process are different from in plants. It was indeed observed that although a large part of LHCII functionally disconnects from PSII during the state 1 to state 2 transition, only part of it associates with PSI, whereas the rest gets quenched (27, 28, 30). However, due to the complexity of the cells and the presence of different LHCII pools, a conclusion about excitation energy transfer efficiency from Lhcb to PSI could not be made.

PSI-LHCI-LHCII supercomplexes with different antenna size have been purified (31–34). The antenna size depends on the method used to induce the state transition and/or on the isolation protocol. The largest PSI-LHCI-LHCII isolated so far contains seven Lhcb (two LHCII trimers and one monomer located on the PsaH/L side of the core complex), in addition to the nine Lhca located on the other side of the core complex (34). This PSI-LHCI-LHCII is clearly larger than the PSI-LHCI-LHCII from plants that contains only one LHCII trimer (35, 36), although recent results indicate that in the membrane of plants, more than one LHCII trimer can be associated with PSI-LHCI (37).

In this work, we have performed time-resolved fluorescence measurements on the PSI-LHCI-LHCII complex of *C. reinhardtii* with or without preferential excitation of Lhcb. We have determined the energy transfer efficiency of these Lhcb and their influence on the trapping yield of PSI. The data indicate a loose connection between the Lhcb and the PSI core, which is responsible for a relatively slow energy transfer step. These results are interpreted on the bases of the new PSI-LHCI structures (14, 15), and the possible energy transfer pathways in PSI-LHCI-LHCII are discussed.

Experimental Procedures

Sample Preparation—PSI-LHCI-LHCII was prepared as in Ref. 34 from the PSII-lacking mutant F139 of *C. reinhardtii* (34, 38, 39). In short, cells were harvested in mid-logarithmic phase (growth at 25 °C, 20 microeinsteins \times m⁻² s⁻¹) and state 2 was induced by incubating them in anaerobic conditions (*i.e.* shaken in the dark for 20 min in the presence of NaN₃). Thyla-

koid membranes were solubilized to a final concentration of 0.5 mg of chlorophyll/ml, 0.5% Digitonin (Sigma), and 0.2% dodecyl- α -D-maltoside, and then loaded on a sucrose gradient. PSI-LHCI-LHCII was harvested with a syringe.

Light-harvesting complexes II (Lhcb) were prepared as in Ref. 12. Band 2 from the sucrose gradient contained Lhcb monomers such as CP26, CP29 and LhcbMs, and Band 3 contained LHCII trimers.

Fraction of Excitation in Lhcb—To selectively excite Lhcb, we determined the fraction of excitation in Lhcb and chose excitation wavelengths for the time-resolved measurements that showed the largest differences. Lhcb were excited the least upon 400 nm with 27–29% of PSI-LHCI-LHCII excitation present in the Lhcb, whereas Lhcb were excited the most upon 475 nm excitation corresponding to 41–46% of the excitation. To determine the fraction, we used two different methods as described in Ref. 40. For details, see SII.

Steady State and Time-resolved Measurements—The absorption spectra were measured at room temperature with a Varian Cary 4000 UV-visible spectrophotometer. CD spectra were measured at 10 °C on a Chirascan-Plus CD spectrometer (Applied Photophysics, Surrey, UK). The 10 °C steady state fluorescence spectra were measured with a spectrofluorometer (FluoroLog, Horiba Scientific) upon 500 nm excitation. To avoid self-absorption, the sample was diluted to optical density 0.07 at the Q_y maximum (1-cm path length) in a buffer containing 20 mM Hepes (pH 7.5) and 0.02% digitonin (Sigma).

Time-resolved fluorescence measurements were performed with a streak camera setup as described in Ref. 40. In short, fs pulses were generated with a repetition rate of 250 kHz using a laser system (Coherent Vitesse Duo and Coherent RegA 9000) and were used to feed the OPA (Coherent OPA 9400) to generate excitation light at 475 and 400 nm. The pulse energy was reduced to 0.3 nJ to avoid singlet-singlet annihilation. The exciting light focused on the sample was 0.151 mol of photons/m²/s at 475 nm and 0.127 mol of photons/m²/s at 400 nm. Fluorescence was detected at the magic angle with respect to the excitation polarization, in the 590–860 nm range from 0 to 400 ps. The sample was measured at 15 °C in its purification buffer (20 mM Hepes, pH 7.8, 0.02% digitonin, 0.7 M sucrose) in a 10 \times 10-mm quartz cuvette at optical density 0.35 cm⁻¹ at the Q_y maximum. To avoid self-absorption, the laser beam was focused in the sample close to the cuvette wall, and emission was collected at a right angle close to the entry point of the laser beam into the cuvette. The sample was stirred with a magnet bar to avoid singlet-triplet annihilation. A power study confirmed the absence of annihilation (data not shown).

The fluorescence decays measured upon 400 and 475 nm excitation were analyzed with a sequential model (see SII). The average decay time τ_{av} (Equation SII-1) characterizes the time for the excitation energy to be used for charge separation and is calculated by considering only the components attributed to the PSI-LHCI-LHCII kinetics (excluding ns components attributed to disconnected species). For more details on the acquisition and data analysis, see SII.

Target Analysis—We used the previous kinetic model describing *C. reinhardtii* PSI-LHCI (see Fig. 3a) (40) and extended it with a new compartment representing the seven

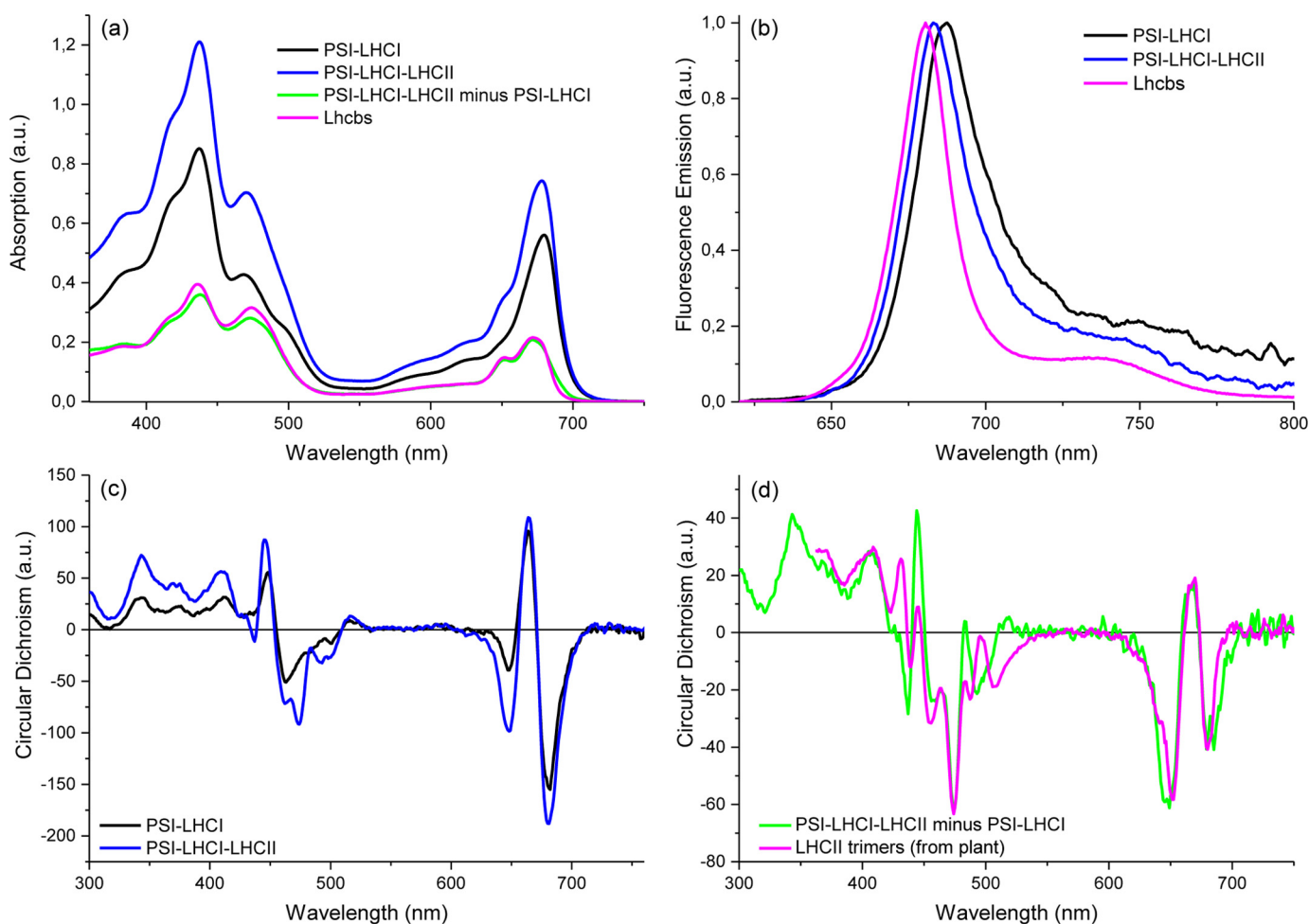


FIGURE 1. **Absorption and emission and CD spectra.** *a*, absorption at room temperature of PSI-LHCI (black) and PSI-LHCI-LHCII (blue) (scaled to their Chl content, see S11) and their difference spectrum (green). The difference spectrum overlaps well with the absorption spectrum of Lhcbs from *C. reinhardtii* (magenta) (scaled LHCII trimer absorption) $\times 2 +$ (scaled Lhcb monomer) $\times 1$. *b*, fluorescence emission spectra at 10 °C of PSI-LHCI and PSI-LHCI-LHCII, both upon 500 nm excitation, and of Lhcbs (isolated monomers) upon 475 nm excitation. The spectra are normalized to their maximum. *c*, CD spectra at 10 °C of PSI-LHCI and PSI-LHCI-LHCII (normalized to the absorption scaled to the Chl content). *d*, the difference spectrum between the CD spectra of PSI-LHCI and PSI-LHCI-LHCII is compared with the CD spectrum of LHCII trimers from plants (measured after solubilization of thylakoid membranes in dodecyl- α -D-maltoside (42)). *a.u.*, arbitrary units.

Lhcbs (called “Lhcb”) in equilibrium with “Bulk” (see Fig. 3*b*). The natural decay rate constant of Lhcb was fixed to k_0' (3.3 ns^{-1}) as found for isolated LHCII trimers of *C. reinhardtii* (41).

The complete kinetic scheme (Scheme SI2-1) also contains precursors populating the other compartments on the ps time scale, with relative amounts varying depending on excitation wavelength (Table SI1-2), and a disconnected compartment corresponding to species with ns lifetimes. A detailed description of the procedure for the target analysis is given in S11.

Simulated Kinetic Models—Population dynamics were simulated (MathWorks R2014b 64-bit, MATLAB) for hypothetical particles of: 1) different size (number of Chls *a*); 2) different connectivity; and 3) different composition (energy of Chls) (Scheme SI3-1). This enabled us to independently study the effects of these three factors on trapping time and efficiency. See SI3 for details.

Distance Measurements in the Reconstructed PSI-LHCI-LHCII—PSI-LHCI-LHCII EM of higher plants (36) and *C. reinhardtii* (34) were used to position the apoproteins of PSI and Lhcbs. The positions were set as close as possible to the EM, but uncertainties remain concerning the exact distance that separates the

apoproteins and their relative orientation. The reconstruction was made with the PyMOL Molecular Graphics System (Version 1.3) to have a three-dimensional perspective and a first estimation of distances between the Chls of interest.

Results

Steady State Characterization—Absorption and fluorescence emission spectra of PSI-LHCI-LHCII are shown in Fig. 1, *a* and *b*, together with the spectra of PSI-LHCI. The maximum Q_y absorption of PSI-LHCI-LHCII (at 678 nm) as well as its maximum emission (at 683 nm) are blue-shifted as compared with the PSI-LHCI maxima (at 679.5 and 687.5 nm, respectively). The absorption difference spectrum between PSI-LHCI-LHCII and PSI-LHCI (Fig. 1*a*, green) overlaps well with the Lhcbs absorption spectrum (Fig. 1*a*, magenta) in agreement with previous results (34).

CD spectra of PSI-LHCI-LHCII and PSI-LHCI are compared in Fig. 1*c*. They show similar features in the Q_y absorption region (negative peaks at 648 and 680 nm and a positive peak at 664 nm), as well as in the Soret region (similar shape below 423 nm). Major differences are visible between 423 and 532 nm, as

Excitation Energy Transfer in PSI-LHCI-LHCII of *C. reinhardtii*

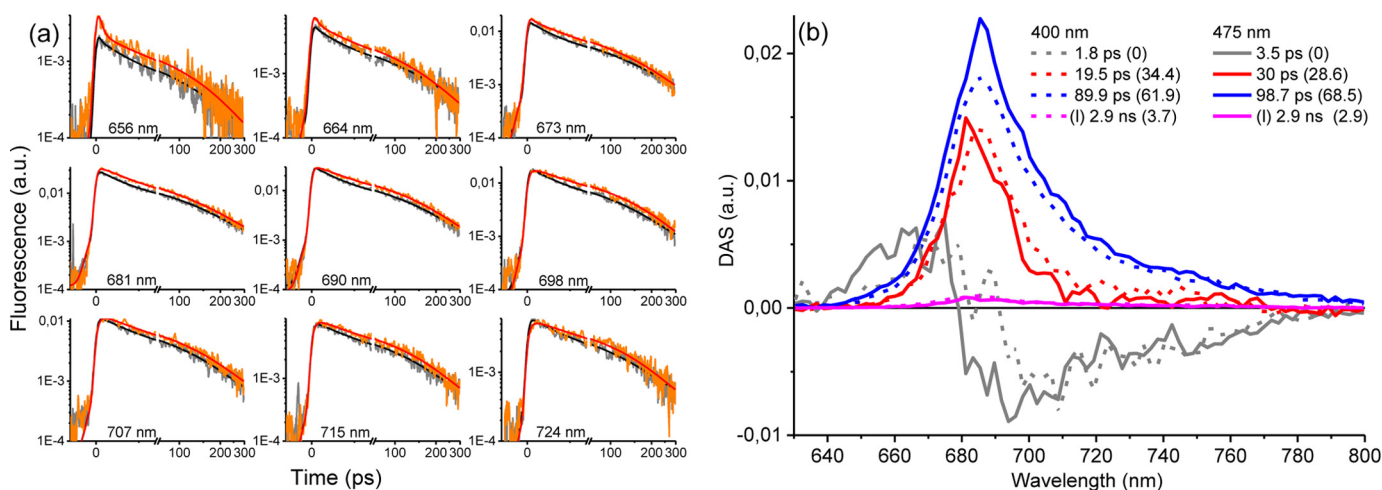


FIGURE 2. Sequential analysis of PSI-LHCI-LHCII fluorescence decays upon 400 nm or 475 nm excitation at 15 °C. *a*, selected fluorescence decay traces after excitation at 400 nm (gray) and 475 nm (orange). Black and red lines indicate the fit curves. *b*, DAS of each decay component. The two different experiments were fitted simultaneously to link (l) the fourth lifetime associated to the disconnected species. The amplitude of each decay component (i.e. relative area = $A_n/\sum_r A_n$) is shown in parentheses next to the corresponding lifetime, in %. The DAS are normalized to the initial populations of excited states (i.e. the total area of PSI-LHCI-LHCII-related DAS, $\sum_r A_n$). See S11 for details. *a.u.*, arbitrary units.

shown in the PSI-LHCI-LHCII minus PSI-LHCI difference spectrum (Fig. 1*d*, green). This spectrum strongly resembles the spectrum of LHCII trimers in detergent micelles (42) but also has some feature of aggregated LHCII trimers (distinct negative peak at 438 nm and positive peak at 483 nm (43)). This suggests that the Lhcb's are involved in additional (or modified) excitonic interactions and/or that as compared with the detergent, LHCII trimers associated with PSI-LHCI are present in a slightly different conformation similar to LHCII trimers in aggregates.

Excitation Energy Transfer and Trapping Kinetics—In this preparation, Lhcb's have been shown to be functionally associated to PSI-LHCI-LHCII (34). To characterize the excitation energy transfer and trapping kinetics of PSI-LHCI-LHCII and estimate the energy transfer rate between Lhcb's and PSI-LHCI, time-resolved fluorescence of PSI-LHCI-LHCII was measured with a streak camera set-up. In *C. reinhardtii*, as in higher plants, the PS core antenna contains only Chl *a*, whereas the peripheral antenna also contains Chl *b*. Excitation in the Chl *a* and in the Chl *b* region can then be used to disentangle the contributions of the core and peripheral antennas (44). More specifically, upon 475 nm excitation, 41–46% of the energy was in Lhcb's, whereas this value dropped to 27–29% upon 400 nm excitation. These two excitation wavelengths were chosen for the time-resolved measurements.

Global Sequential Analysis—The fluorescence decays measured upon 400 and 475 nm excitation were analyzed with a sequential model. The data can be well described by a minimum of four components (no structure in the residuals, Fig. 2). A clear difference between both excitation wavelengths is observed in the decay of PSI-LHCI-LHCII at an early time where fast Chl *b* decay is clearly visible after their preferential excitation at 475 nm (see in particular 656 nm in Fig. 2*a*). The decay-associated spectra (DAS) for both excitation wavelengths are shown in Fig. 2*b*. The first component is a pure energy transfer component (conservative positive-negative shape of the DAS) from blue Chl's (*a* and *b*) to red Chl's *a* for both excitation wavelengths. This transfer is faster at 400 nm

than at 475 nm (1.8 ps as compared with 3.5 ps, respectively), possibly because of an additional transfer step occurring from Chl's *b* to blue Chl's *a* upon 475 nm where Chl's *b* are preferentially excited. Indeed, the Chl's *b* emission at ~650 nm appears in the DAS of this fast component upon 475 nm excitation. The next two components are mainly decay components for both excitation wavelengths, with faster lifetimes upon 400 nm excitation as compared with 475 nm (~20/~90 ps as compared with ~30/100 ps, respectively). The fourth component has very small amplitude (~3–4%) and represents disconnected Lhcb's/Lhcb's/Chl's with ns lifetime (41, 45). Fit parameters are summarized in Fig. 2*b*.

The average decay time τ_{av} of PSI-LHCI-LHCII is ~65 ps upon 400 nm and ~78 ps upon 475 nm. The association of Lhcb's increases the average decay time by ~15 ps at 400 nm and by ~27 ps at 475 nm as compared with the average decay times of PSI-LHCI (49.7 and 51.4 ps, respectively (40)).

Target Analysis—To estimate the energy transfer rate between PSI-LHCI and LHCII within PSI-LHCI-LHCII, a target analysis was performed on the two datasets (400 and 475 nm excitation) simultaneously. The previous kinetic scheme reported in Ref. 40 (Fig. 3*a*) was used to model PSI-LHCI-related kinetics, and the Lhcb's were modeled by an extra compartment (called “Lhcb”) transferring energy to the “Bulk” compartment (Fig. 3*b*). Several constraints were imposed on the fit parameters (rate constants, species-associated spectra (SAS), and initial populations) as described in S11-iii. An additional compartment (Scheme S12-1) accounts for a small population of disconnected species (~3%) whose lifetime (3.2 ns) is very close to that of the Lhcb's in *C. reinhardtii* (41).

The kinetic model (Fig. 3*b*) fits the data well (Fig. S12-1). Rate constants fitted from the target are given in Fig. 3*b* (in red), and the SAS are given in Fig. 4. The Lhcb SAS has a significantly lower red emission and a narrower bandwidth as compared with Bulk as expected (Fig. 4 and Fig. S12-2*b*). The red shift visible in the Lhcb SAS as compared with the isolated Lhcb steady state emission spectrum (Fig. 4) suggests that Lhcb's

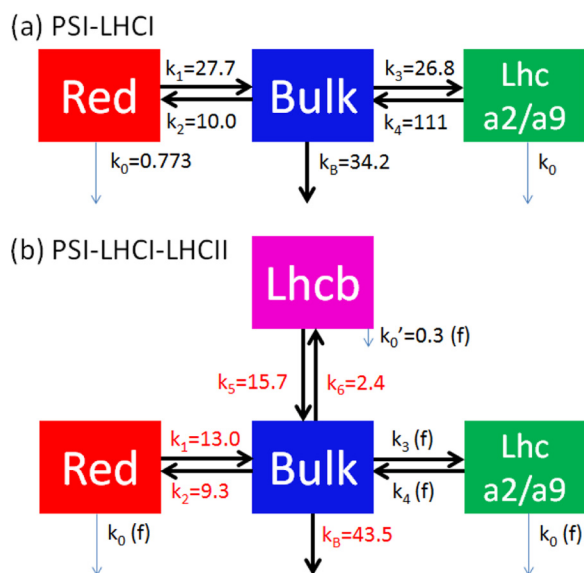


FIGURE 3. Kinetic models for target analysis of PSI-LHCI (a) and of PSI-LHCI-LHCII (b), with the rate constants (in ns^{-1}). Rate constants are either fitted (indicated in red) or fixed (indicated in black). Both supercomplexes have similar relative initial population in Red, Bulk and Lhca2/a9 compartments. In b, there is additional initial population on Lhcb. See S11 for details.

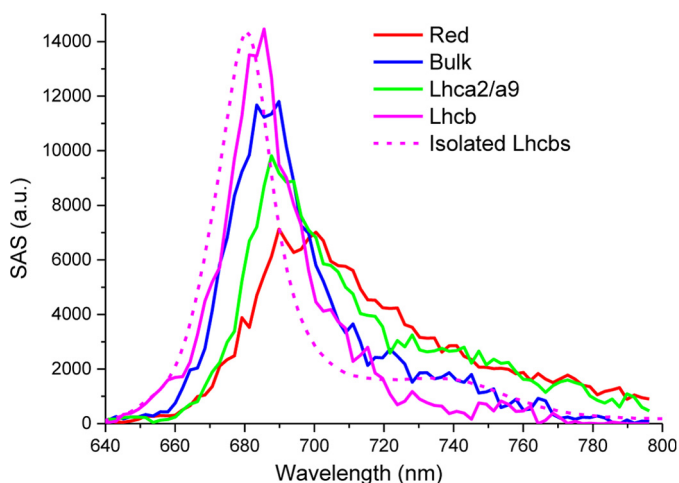


FIGURE 4. Estimated SAS of each compartment and comparison with the steady state emission spectrum of Lhcbs (isolated monomers, dashed magenta normalized to Lhcb SAS maximum). The SAS are constrained to an equal area. Precursors and disconnected compartment SAS are presented in Fig. S12-2. a. u., arbitrary units.

associated with PSI are in a different conformation than when isolated in detergent, in agreement with the CD spectra. The free energy difference ΔG between Bulk and Lhcb is estimated, according to Equation 1, at -48 meV.

$$\Delta G = G_{\text{Bulk}} - G_{\text{Lhcb}} = -k_B T \times \ln\left(\frac{k_5}{k_6}\right) \quad (\text{Eq. 1})$$

It corresponds to an enthalpy difference ΔH of -21 meV ($\Delta H = \Delta G + T\Delta S = H_{\text{Bulk}} - H_{\text{Lhcb}} = -k_B T \times \ln(N_{\text{Lhcb}}/N_{\text{Bulk}} \times k_5/k_6)$) with 147 Chls *a* estimated in Bulk, see S12-iv, and 55 Chls *a* in Lhcb, Table S11-1). This enthalpy difference corresponds to an ~ 9 -nm blue shift of Lhcb as compared with Bulk.

The amplitude matrices (Table 1 upon 475 nm and Table S12-1 upon 400 nm excitation) detail the extent of (de)population of

TABLE 1

Amplitude matrices of PSI-LHCI-LHCII upon 475 nm excitation and the overall amplitude of the trapping at each lifetime

Lifetimes	PSI-LHCI-LHCII (475 nm excitation)				Overall amplitude of the trapping
	Red	Bulk	Lhca2/a9	Lhcb	
<i>ps</i>					
1.0	0.000	0.008	0.000	-0.447	0.000
1.1	-0.054	-0.491	0.016	0.001	-0.023
1.4	0.000	0.011	-0.065	0.000	0.001
6.5	-0.007	0.106	-0.067	-0.002	0.029
22.9	-0.047	0.152	0.059	-0.013	0.151
63.8	-0.308	0.064	0.018	0.397	0.171
97.3	0.416	0.151	0.040	0.063	0.670

each compartment for each lifetime and give the time scale at which Lhcbs transfer energy to the rest of the supercomplex. The three shorter lifetimes do not have large amplitudes in the trapping (overall amplitude ~ 0) and correspond to times where precursors transfer energy to the other four compartments. The ~ 23 -, ~ 64 -, and ~ 97 -ps lifetimes represent trapping components with most of the trapping occurring with the longest lifetime. With an ~ 64 -ps lifetime, Lhcb equilibrates (large positive amplitude) with all the other compartments. Similar observations can be made when exciting PSI-LHCI-LHCII at 400 nm (Table S12-1) except that the ~ 23 -ps lifetime contributes more to the trapping than upon 475 nm. The average decay times obtained by target analysis of PSI-LHCI-LHCII are 70 ps upon 400 nm and 80 ps upon 475 nm excitation (see S11-iii), consistent with the average decay times calculated from the sequential analysis (see above).

Contributions of Antenna Size, Connectivity, and Composition to the Average Decay Time of PSI-LHCI and PSI-LHCI-LHCII—The equilibration time between two compartments is influenced by their size (number of Chls in each compartment), by their composition (energy of the Chls), and by the connectivity between them. To disentangle these different contributions, the kinetics of hypothetical PSI-LHCI and PSI-LHCI-LHCII complexes with different compartment size, composition, and/or connectivity were simulated (Scheme S13-1), and their average decay time was compared (Table S13-1). In the simulation, we have compared the effect of the presence of Lhca2 and Lhca9, the most loosely bound antenna complexes of PSI (18), with that of the seven Lhcbs. The simulations show that: 1) The addition of 16 Chls *a* (as many as initially contained in Lhca2 and Lhca9, see Table S11-1 and S12-iv) when isoenergetic with the bulk slows down the average decay time by ~ 2.5 ps, while the addition of 55 Chls *a* (as many as initially contained in the seven Lhcbs, see Table S11-1) slows it down by 4–6 ps. 2) The connectivity of PSI with Lhca2 and Lhca9 is very good and does not influence the average decay time of PSI-LHCI, whereas the connectivity between PSI-LHCI and Lhcbs is not optimal and is responsible for an increase of the decay time of 16–25 ps as compared with the best possible case. 3) The red forms contained in Lhca2 and Lhca9 (46) slow down the kinetics of PSI-LHCI by ~ 5 ps, whereas the bluer Chls in Lhcbs (as compared with bulk Chls of PSI-LHCI) speed up the kinetics by 2–3 ps. A detailed description of the simulations is presented in S13.

Discussion

Time-resolved measurements of the PSI-LHCI-LHCII complex of *C. reinhardtii*, the largest PSI supercomplex isolated so

Excitation Energy Transfer in PSI-LHCI-LHCII of *C. reinhardtii*

far (34), show that the trapping time of this supercomplex is ~ 65 ps upon 400 nm excitation and ~ 78 ps upon 475 nm excitation (Table 2). This large difference between the two excitation wavelengths is attributed to the differential excitation of Lhcbs (more Lhcb excitation at 475 nm, see Table S11-2). This implies that the transfer from Lhcbs to PSI-LHCI is slow relative to the trapping within PSI-LHCI. The presence of seven

Lhcbs slows down the overall trapping by 15 ps at 400 nm and by 27 ps at 475 nm excitation (Table 2). This result helps in interpreting the time-resolved data on *C. reinhardtii* *in vivo* (27). If a large population of PSI-LHCI-LHCII particles should be expected in the cells in state 2 as compared with state 1, not only a large difference in the amplitude of the PSI component should be observed but also a significant difference in its lifetime. The fact that none of these effects were observed in the time-resolved measurements in the cells indicates that the difference in the amount of LHCII associated with PSI in state 1 and 2 is relatively small as concluded by Ünlü *et al.* (27).

The detailed modeling of the measurements (Fig. 3b) shows that the excitation energy transfer between Lhcbs and the rest of the supercomplex occurs in ~ 60 ps (Table 1). Several factors can influence the transfer rates: the antenna size, the energy of the pigments associated with the complexes, and the connectivity between Lhcbs and PSI-LHCI. To discriminate between

TABLE 2

Average decay times and trapping efficiencies of PSI-LHCI-LHCII compared to PSI-LHCI

$\tau_{\text{no CS}}$ is the average decay time in the (hypothetical) case that charge separation (CS) cannot occur. $\tau_{\text{no CS}}$ is approximated as the average decay time of plant Lhca monomer (~ 2 ns), the closest system of PSI-LHCI where charge separation does not occur.

	PSI-LHCI (40)		PSI-LHCI-LHCII	
Excitation wavelength (in nm)	400	475	400	475
Average decay time τ_{av} (in ps)	49.7	51.4	64.8	78.4
Trapping efficiency (52)	97.5%	97.4%	96.7%	96.0%
$(\Phi_{\text{CS}} = 1 - \tau_{\text{av}}/\tau_{\text{no CS}})$				

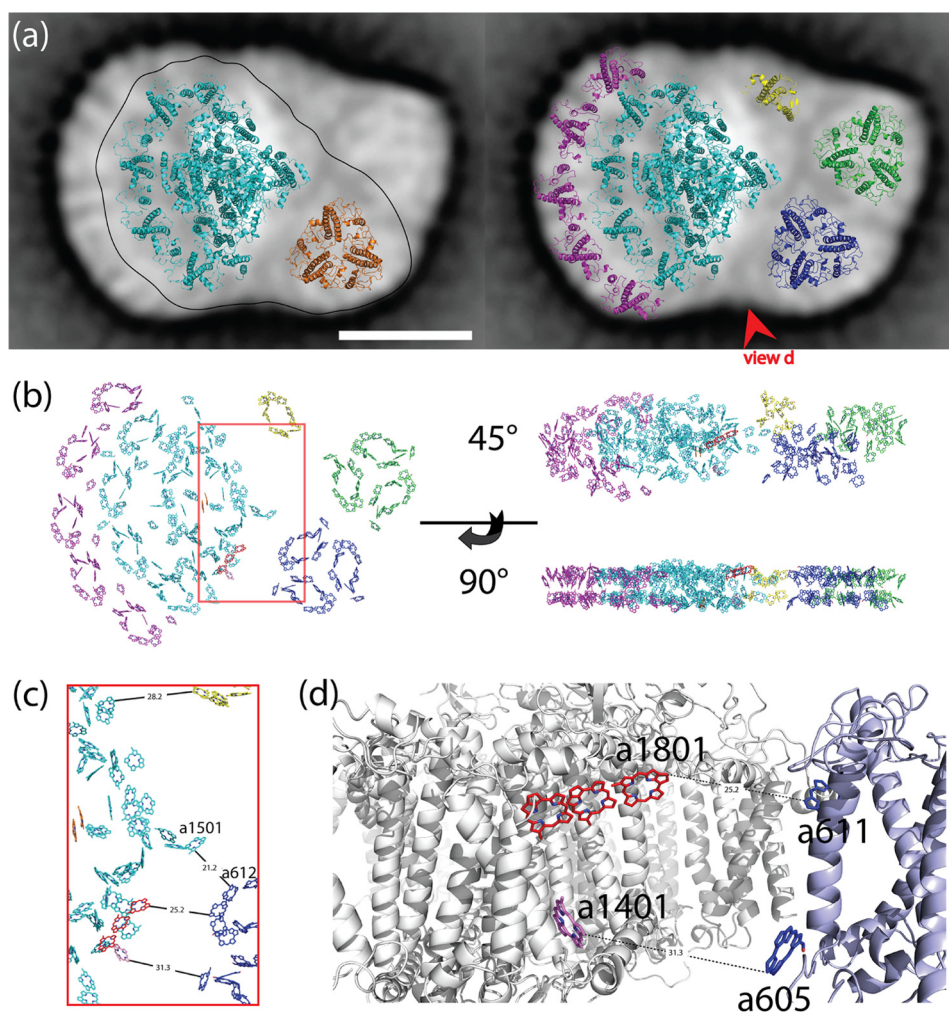


FIGURE 5. *a*, EM images of PSI-LHCI-LHCII from *C. reinhardtii* (34) viewed from the stromal side superimposed with apoproteins of PSI-LHCI of higher plants in cyan (Protein Data Bank (PDB) 4XK8 (14)) and LHCII trimer in brown (PDB 1RWT (20)) assembled as PSI-LHCI-LHCII of higher plants (black outline of EM of *A. thaliana* (36)) (left); or superimposed with LHCII assembled as PSI-LHCI-LHCII of *C. reinhardtii* by slightly rotating the LHCII trimer in brown into the LHCII trimer in blue and by adding a new LHCII trimer in green, CP29 in yellow (PDB 3PL9 (6)), and the five additional Lhcbs present in *C. reinhardtii* in magenta (duplicates of Lhca1 from Ref. 14) (right). The scale bar is 10 nm. The reconstruction was made with PyMOL. *b*, three-dimensional views of porphyrin rings from Chls bound to the apoproteins presented in *a* (right) with the same color: view from the stromal side (left) rotated 45° (upper right) or 90° (lower right) along the black axis. *c*, selection of the Chls present at the interface of Lhcbs and PSI core (1.8 \times magnification of the red frame in *b*). The shortest distances between the closest atoms of the porphyrin rings of PSI Chls and Lhcbs Chls are indicated in Å for the different sides of PSI core. *d*, Chls *a* trimer (red) binding PsaA (apoprotein in gray) and Chl *a*1401 (pink) newly found in Ref. 14, viewed from the side indicated with a red arrow in *a* (right). These Chls could be involved in energy transfer pathways with LHCII (apoprotein in light blue).

the contributions of these factors to the trapping time of PSI-LHCI and PSI-LHCI-LHCII, we have simulated excited state population dynamics of hypothetical particles where each factor was controlled. The connectivity of the Lhcbs was compared with that of the most loosely bound Lhcas (Lhca2 and Lhca9) (18), which also show a relatively slow equilibration (~ 7 ps) with the rest of the complex (40). The results indicate that the functional connectivity between Lhca2/a9 and the PSI complex is very high and that the observed relatively slow migration is due to the presence of low energy forms (46) in these Lhcas. This conclusion is in agreement with the observation that the presence of red forms slows down the trapping kinetics in different organisms (40, 47–49). On the contrary, the results show that in PSI-LHCI-LHCII the favorable downhill energy transfer profile of Lhcbs cannot compensate their low connectivity with PSI core. This low connectivity largely explains the slow transfer from Lhcbs to the PSI core and can be due to a low number of transfer pathways.

To determine the possible transfer pathways in the PSI-LHCI-LHCII, we reconstructed its three-dimensional structure by mapping the structures of LHCII trimer (20), CP29 (6), and PSI-LHCI (14, 15) of higher plant onto the EM projection map of PSI-LHCI-LHCII of *C. reinhardtii* (34). The structure of all subunits of *C. reinhardtii* is expected to be similar to that of higher plants given the sequence similarity (50, 51). Different views of the structural model are presented in Fig. 5.

Using the reconstructed model of the supercomplex, we looked for the shortest distances between the Chls of Lhcbs and those of the PSI core (Fig. 5, *b* and *c*), which should represent possible energy transfer pathways. We could not identify pairs of Chls that are separated by less than 18 Å (nearest edge-to-edge distance), in line with the slow energy transfer between Lhcbs and PSI core observed in the measurements. The shortest distances are observed between Chl *a*612 of one LHCII trimer (which is in a similar position as in PSI-LHCI-LHCII of higher plant, and is depicted in *blue* in Fig. 5, nomenclature for LHCII Chls from (20)) and two PSI core Chls: Chl *a*1501 (nomenclature for the core Chls from Ref. 14, distance ~ 21 Å) bound to PsaL and the additional Chl (distance ~ 18 Å) associated with PsaH, which is only present in the structure of Mazor *et al.* (15) (PDB 4Y28, Chl designated as H1 in this structure). The next shortest distance is ~ 25 Å and involves Chl *a*611 of the same LHCII trimer and Chl *a*1801, belonging to a PsaA Chl trimer that was proposed to connect PSI and LHCII trimer in plants in Ref. 15. Other pathways suggested in Refs. 14 and 15 involve Chl *a*1401 (coordinated to PsaA on the luminal side, Fig. 5, *c* and *d*) and Chl *a*1403 (coordinated to PsaK, Fig. 5, *c* and *d*) but are not expected to play a major role given the large distances that separate them from the Chls of LHCII (>30 Å). Similarly, PSI Chls are very far from the second LHCII trimer (depicted in *green* in Fig. 5, with Chl *a*612 at a distance of ~ 45 Å from Chl *a*1501 in Ref. 14 or ~ 37 Å from H1 in Ref. 15) as well as from the Lhcb monomer (Fig. 5*c*).

The three-dimensional reconstruction should be considered with some caution as the distances between the Chls can only be approximately estimated due to the low resolution of the EM maps, and the presence of one or two additional Chls in between the complexes cannot be completely excluded. How-

ever, it is clear that the gap between LHCII and the PSI core is rather large, and only a few energy transfer pathways seem to be available in agreement with the experimental results. The large distance between the Chls of PSI and LHCII also indicates that the observed differences in the CD signal between the sum of PSI-LHCI and LHCII spectra and the spectrum of the PSI-LHCI-LHCII complex are likely due to a different conformation assumed by LHCII when associated with PSI and not to the presence of new excitonic interactions between Chls of LHCII and PSI core.

It should be noticed that the observed loose connectivity between LHCII and PSI core has a small influence on the trapping efficiency of PSI-LHCI-LHCII. Indeed, even with a 43% increase in the number of Chls (Table SII-1), the trapping yield of PSI-LHCI-LHCII is as high as 96% (Table 2) (52), only 1.4% lower than in the absence of Lhcbs. The 43% increase in Chls corresponds to an increase of the absorption cross section by 47% (averaged over the spectral range), which can make a significant difference in terms of light-harvesting capacities, especially under low light conditions. In this respect, it is interesting to notice the very large difference in efficiency and flexibility between PSI and PSII. We have previously estimated that 240 Chls *a* per RC represent a maximal antenna size for PSII because above this value the increase in light harvesting would be compensated by the slow migration toward the RC, resulting in an effective loss of efficiency (53). This is clearly not the case for PSI, which is able to accommodate a very large antenna, maintaining a high efficiency even in the presence of slow transfer. Indeed, the results presented here show that in PSI-LHCI-LHCII of *C. reinhardtii*, which contains 240 Chls *a* per RC, 96 out of 100 photons absorbed lead to charge separation in the RC. The design of PSI seems then to represent the way to go for efficient light harvesting.

Author Contributions—R. C. conceived the research; C. L. Q., B. v. O., and R. C. designed the research, B. D. prepared the samples; C. L. Q. performed all the spectroscopic experiments, the global analysis, and the modelling; and C. L. Q. and I. H. M. v. S. performed the target analysis. B. v. O. and R. C. supervised the research, and C. L. Q. and R. C. wrote the paper with contributions from all the authors. All authors approved the final version of the manuscript.

Acknowledgment—We thank Yuval Mazor for providing the PDB file of his crystal structure of higher plant PSI-LHCI.

References

- Blankenship, R. E. (2014) *Molecular Mechanisms of Photosynthesis*, 2nd Ed., Wiley-Blackwell, Hoboken, NJ
- Croce, R., and van Amerongen, H. (2014) Natural strategies for photosynthetic light harvesting. *Nat. Chem. Biol.* **10**, 492–501
- Jordan, P., Fromme, P., Witt, H. T., Klukas, O., Saenger, W., and Krauss, N. (2001) Three-dimensional structure of cyanobacterial photosystem I at 2.5 Å resolution. *Nature* **411**, 909–917
- Umena, Y., Kawakami, K., Shen, J.-R., and Kamiya, N. (2011) Crystal structure of oxygen-evolving photosystem II at a resolution of 1.9 Å. *Nature* **473**, 55–60
- Hohmann-Marriott, M. F., and Blankenship, R. E. (2011) Evolution of photosynthesis. *Annu. Rev. Plant Biol.* **62**, 515–548
- Pan, X., Liu, Z., Li, M., and Chang, W. (2013) Architecture and function of plant light-harvesting complexes II. *Curr. Opin. Struct. Biol.* **23**, 515–525

7. Ballottari, M., Girardon, J., Dall'osto, L., and Bassi, R. (2012) Evolution and functional properties of Photosystem II light harvesting complexes in eukaryotes. *Biochim. Biophys. Acta* **1817**, 143–157
8. Jansson, S. (1999) A guide to the *Lhc* genes and their relatives in *Arabidopsis*. *Trends Plant Science* **4**, 236–240
9. Minagawa, J., and Takahashi, Y. (2004) Structure, function and assembly of Photosystem II and its light-harvesting proteins. *Photosynthesis Research* **82**, 241–263
10. Dekker, J. P., and Boekema, E. J. (2005) Supramolecular organization of thylakoid membrane proteins in green plants. *Biochim. Biophys. Acta* **1706**, 12–39
11. Tokutsu, R., Kato, N., Bui, K. H., Ishikawa, T., and Minagawa, J. (2012) Revisiting the supramolecular organization of photosystem II in *Chlamydomonas reinhardtii*. *J. Biol. Chem.* **287**, 31574–31581
12. Drop, B., Webber-Birungi, M., Yadav, S. K. N., Filipowicz-Szymanska, A., Fusetti, F., Boekema, E. J., and Croce, R. (2014) Light-harvesting complex II (LHCII) and its supramolecular organization in *Chlamydomonas reinhardtii*. *Biochim. Biophys. Acta* **1837**, 63–72
13. Ben-Shem, A., Frolow, F., and Nelson, N. (2003) Crystal structure of plant photosystem I. *Nature* **426**, 630–635
14. Qin, X., Suga, M., Kuang, T., and Shen, J.-R. (2015) Structural basis for energy transfer pathways in the plant PSI-LHCI supercomplex. *Science* **348**, 989–995
15. Mazor, Y., Borovikova, A., and Nelson, N. (2015) The structure of plant photosystem I super-complex at 2.8 Å resolution. *Elife* **4**, e07433
16. Takahashi, Y., Yasui, T. A., Stauber, E. J., and Hippler, M. (2004) Comparison of the subunit compositions of the PSI-LHCI supercomplex and the LHCI in the green alga *Chlamydomonas reinhardtii*. *Biochemistry* **43**, 7816–7823
17. Stauber, E. J., Busch, A., Naumann, B., Svatoš, A., and Hippler, M. (2009) Proteotypic profiling of LHCI from *Chlamydomonas reinhardtii* provides new insights into structure and function of the complex. *Proteomics* **9**, 398–408
18. Drop, B., Webber-Birungi, M., Fusetti, F., Kouil, R., Redding, K. E., Boekema, E. J., and Croce, R. (2011) Photosystem I of *Chlamydomonas reinhardtii* contains nine light-harvesting complexes (Lhca) located on one side of the core. *J. Biol. Chem.* **286**, 44878–44887
19. Croce, R., and van Amerongen, H. (2013) Light-harvesting in photosystem I. *Photosynth. Res.* **116**, 153–166
20. Liu, Z., Yan, H., Wang, K., Kuang, T., Zhang, J., Gui, L., An, X., and Chang, W. (2004) Crystal structure of spinach major light-harvesting complex at 2.72 Å resolution. *Nature* **428**, 287–292
21. Wientjes, E., and Croce, R. (2011) The light-harvesting complexes of higher-plant Photosystem I: Lhca1/4 and Lhca2/3 form two red-emitting heterodimers. *Biochem. J.* **433**, 477–485
22. Rochaix, J.-D. (2014) Regulation and dynamics of the light-harvesting system. *Annu. Rev. Plant Biol.* **65**, 287–309
23. Allen, J. F. (2003) State transitions: a question of balance. *Science* **299**, 1530–1532
24. Minagawa, J. (2011) State transitions: the molecular remodeling of photosynthetic supercomplexes that controls energy flow in the chloroplast. *Biochim. Biophys. Acta* **1807**, 897–905
25. Wientjes, E., van Amerongen, H., and Croce, R. (2013) LHCII is an antenna of both photosystems after long-term acclimation. *Biochim. Biophys. Acta* **1827**, 420–426
26. Alloquent, G., Tokutsu, R., Roach, T., Peers, G., Cardol, P., Girard-Bascou, J., Seigneurin-Berny, D., Petroutsos, D., Kuntz, M., Breyton, C., Franck, F., Wollman, F. A., Niyogi, K. K., Krieger-Liszkay, A., Minagawa, J., and Finazzi, G. (2013) A dual strategy to cope with high light in *Chlamydomonas reinhardtii*. *Plant Cell* **25**, 545–557
27. Ünlü, C., Drop, B., Croce, R., and van Amerongen, H. (2014) State transitions in *Chlamydomonas reinhardtii* strongly modulate the functional size of photosystem II but not of photosystem I. *Proc. Natl. Acad. Sci. U.S.A.* **111**, 3460–3465
28. Nagy, G., Ünneper, R., Zsiros, O., Tokutsu, R., Takizawa, K., Porcar, L., Moyet, L., Petroutsos, D., Garab, G., Finazzi, G., and Minagawa, J. (2014) Chloroplast remodeling during state transitions in *Chlamydomonas reinhardtii* as revealed by noninvasive techniques *in vivo*. *Proc. Natl. Acad. Sci. U.S.A.* **111**, 5042–5047
29. Delosme, R., Olive, J., and Wollman, F.-A. (1996) Changes in light energy distribution upon state transitions: an *in vivo* photoacoustic study of the wild type and photosynthesis mutants from *Chlamydomonas reinhardtii*. *Biochim. Biophys. Acta* **1273**, 150–158
30. Włodarczyk, L. M., Snellenburg, J. J., Ihalainen, J. A., van Grondelle, R., van Stokkum, I. H. M., and Dekker, J. P. (2015) Functional rearrangement of the light-harvesting antenna upon state transitions in a green alga. *Biophys. J.* **108**, 261–271
31. Kargul, J., Turkina, M. V., Nield, J., Benson, S., Vener, A. V., and Barber, J. (2005) Light-harvesting complex II protein CP29 binds to photosystem I of *Chlamydomonas reinhardtii* under State 2 conditions. *The FEBS Journal* **272**, 4797–4806
32. Takahashi, H., Iwai, M., Takahashi, Y., and Minagawa, J. (2006) Identification of the mobile light-harvesting complex II polypeptides for state transitions in *Chlamydomonas reinhardtii*. *Proc. Natl. Acad. Sci. U.S.A.* **103**, 477–482
33. Takahashi, H., Okamuro, A., Minagawa, J., and Takahashi, Y. (2014) Biochemical characterization of photosystem I-associated light-harvesting complexes I and II isolated from state 2 cells of *Chlamydomonas reinhardtii*. *Plant Cell Physiol.* **55**, 1437–1449
34. Drop, B., Yadav K. N., S., Boekema, E. J., and Croce, R. (2014) Consequences of state transitions on the structural and functional organization of Photosystem I in the green alga *Chlamydomonas reinhardtii*. *Plant J.* **78**, 181–191
35. Kouřil, R., Zygadlo, A., Arteni, A. A., de Wit, C. D., Dekker, J. P., Jensen, P. E., Scheller, H. V., and Boekema, E. J. (2005) Structural characterization of a complex of photosystem I and light-harvesting complex II of *Arabidopsis thaliana*. *Biochemistry* **44**, 10935–10940
36. Galka, P., Santabarbara, S., Khuong, T. T., Degand, H., Morsomme, P., Jennings, R. C., Boekema, E. J., and Caffarri, S. (2012) Functional analyses of the plant photosystem I-light-harvesting complex II supercomplex reveal that light-harvesting complex II loosely bound to photosystem II is a very efficient antenna for photosystem I in state II. *Plant Cell* **24**, 2963–2978
37. Bell, A. J., Frankel, L. K., and Bricker, T. M. (2015) High yield non-detergent isolation of photosystem I-light-harvesting chlorophyll II membranes from spinach thylakoids: implications for the organization of PSI antennae in higher plants. *J. Biol. Chem.* **290**, 18429–18437
38. Garnier, J., Guyon, D., and Picaud, A. (1979) Characterization of new strains of nonphotosynthetic mutants of *Chlamydomonas reinhardtii*. I. Fluorescence, photochemical activities, chlorophyll-protein complexes. *Plant Cell Physiol.* **20**, 1013–1027
39. Maroc, J., Garnier, J., and Guyon, D. (1989) Chlorophyll-protein complexes related to photosystem I in *Chlamydomonas reinhardtii*. *J. Photochem. Photobiol. B* **4**, 97–109
40. Le Quiniou, C., Tian, L., Drop, B., Wientjes, E., van Stokkum, I. H. M., van Oort, B., and Croce, R. (2015) PSI-LHCI of *Chlamydomonas reinhardtii*: Increasing the absorption cross section without losing efficiency. *Biochim. Biophys. Acta* **1847**, 458–467
41. Natali, A., and Croce, R. (2015) Characterization of the major light-harvesting complexes (LHCBM) of the green alga *Chlamydomonas reinhardtii*. *PLoS ONE* **10**, e0119211
42. Georgakopoulou, S., van der Zwan, G., Bassi, R., van Grondelle, R., van Amerongen, H., and Croce, R. (2007) Understanding the changes in the circular dichroism of light harvesting complex II upon varying its pigment composition and organization. *Biochemistry* **46**, 4745–4754
43. Akhtar, P., Dorogi, M., Pawlak, K., Kovács, L., Bóta, A., Kiss, T., Garab, G., and Lambrev, P. H. (2015) Pigment interactions in light-harvesting complex II in different molecular environments. *J. Biol. Chem.* **290**, 4877–4886
44. van Oort, B., Amunts, A., Borst, J. W., van Hoek, A., Nelson, N., van Amerongen, H., and Croce, R. (2008) Picosecond fluorescence of intact and dissolved PSI-LHCI crystals. *Biophys J* **95**, 5851–5861
45. Passarini, F., Wientjes, E., van Amerongen, H., and Croce, R. (2010) Photosystem I light-harvesting complex Lhca4 adopts multiple conformations: red forms and excited-state quenching are mutually exclusive. *Biochim. Biophys. Acta* **1797**, 501–508

46. Mozzo, M., Mantelli, M., Passarini, F., Caffarri, S., Croce, R., and Bassi, R. (2010) Functional analysis of Photosystem I light-harvesting complexes (Lhca) gene products of *Chlamydomonas reinhardtii*. *Biochim. Biophys. Acta* **1797**, 212–221
47. Gobets, B., van Stokkum, I. H. M., Rögner, M., Kruip, J., Schlodder, E., Karapetyan, N. V., Dekker, J. P., and van Grondelle, R. (2001) Time-resolved fluorescence emission measurements of photosystem I particles of various cyanobacteria: a unified compartmental model. *Biophys. J.* **81**, 407–424
48. Jennings, R. C., Zucchelli, G., Croce, R., and Garlaschi, F. M. (2003) The photochemical trapping rate from red spectral states in PSI-LHCI is determined by thermal activation of energy transfer to bulk chlorophylls. *Biochim. Biophys. Acta* **1557**, 91–98
49. Wientjes, E., van Stokkum, I. H. M., van Amerongen, H., and Croce, R. (2011) The role of the individual Lhcas in photosystem I excitation energy trapping. *Biophys. J.* **101**, 745–754
50. Hippler, M., Rimbault, B., and Takahashi, Y. (2002) Photosynthetic complex assembly in *Chlamydomonas reinhardtii*. *Protist* **153**, 197–220
51. Allen, J. F., de Paula, W. B., Puthiyaveetil, S., and Nield, J. (2011) A structural phylogenetic map for chloroplast photosynthesis. *Trends Plant Sci.* **16**, 645–655
52. van Amerongen, H., Valkunas, L., and van Grondelle, R. (2000) *Photosynthetic Excitons*, pp. 401–478, World Scientific, Singapore
53. Wientjes, E., van Amerongen, H., and Croce, R. (2013) Quantum yield of charge separation in photosystem II: functional effect of changes in the antenna size upon light acclimation. *J. Phys. Chem. B* **117**, 11200–11208

The high efficiency of Photosystem I in the green alga *Chlamydomonas reinhardtii* is maintained after the antenna size is substantially increased by the association of Light Harvesting Complex II

Clotilde Le Quiniou, Bart van Oort, Bartłomiej Drop, Ivo H. M. van Stokkum and Roberta Croce

SI1: Materials and Methods

i. Methods to determine the fraction of excitation in Lhcbs

In short, the first method calculates the absorption of Lhcbs relative to PSI-LHCI-LHCII by estimating the relative difference of their absorption spectra scaled in the Q_y region to their chlorophylls (Chls) content (Table SII-1 and explanation below) and considering an oscillator strength ratio of 0.7 between Chl *b* and Chl *a* (1). The second method calculates the absorption cross section of both Lhcbs and PSI-LHCI-LHCII by using the extinction coefficients of the individual pigments (2) corrected by an energy transfer efficiency of 70% for the carotenoids (Cars) (3,4).

To scale the absorption spectra of PSI-LHCI-LHCII to its Chls content and to calculate its absorption cross section, we estimate the number of pigments in *C. reinhardtii* (Table SII-1). The total number of Chls in PSI-LHCI-LHCII of *C. reinhardtii* was obtained by adding to the 155 Chls of the PSI-LHCI of higher plant (5) (i) 70 Chls to account for the 5 additional Lhcas present in PSI-LHCI of *C. reinhardtii* (6) assuming an average of 14 Chls in each Lhca (5,7) and (ii) 97 Chls to account for the 7 additional Lhcbs associated with PSI-LHCI (8) calculated by assuming 13 Chls in the monomer (9) and 42 Chls per LHCII trimer (10). The number of Car per Lhcas and Lhcbs of *C. reinhardtii* were assumed as in higher plant: with 3 in Lhca (5,11), 3 in Lhcb monomer (9) and 12 in LHCII trimer (10), for a total of 76 Cars present in PSI-LHCI-LHCII of *C. reinhardtii* (Table SII-1).

	PSI-LHCI	Lhcbs	PSI-LHCI-LHCII
Number of Lhcas	9	-	9
Number of Lhcbs	-	7 (1 monomer + 2 trimers)	7
Chls <i>a</i> +Chls <i>b</i>	225	97	322
Chls <i>a</i> /Chls <i>b</i>	4.4±0.1 (6)	Monomer: 1.29±0.06 Trimer: 1.28±0.02 (12)	2.95 ±0.05 (8)
Chls <i>a</i>	183	55	241
Chls <i>b</i>	42	42	81
Carotenoids	49	27	76

Table SII-1: Estimation of the number of Chls and Cars in PSI-LHCI, PSI-LHCI-LHCII and Lhcbs.

The initial excitation energy in Lhcbs ranges between 27%-29% upon 400 nm excitation and 41%-46% upon 475 nm excitation.

ii. Sequential analysis of the time-resolved measurements

Each experiment (one at each excitation wavelength) consists of a sequence of 20 images of 3 min each, acquired in HPD-TA 8.4.0 (Hamamatsu). Image sequences were corrected for background, shading and jitter (temporal drift between images within an image sequence) and finally averaged in HPD-TA 8.4.0 (Hamamatsu). These corrected datasets were binned to 2 nm, and zoomed between 640 nm and 800 nm in Glotaran 1.3 (13).

Each dataset was analyzed globally with a sequential model (14-16) in Glotaran 1.3. The Decay Associated Spectra (DAS) were calculated from the Evolution Associated Spectra (EAS) directly obtained after sequential analysis. The IRF was modeled as the sum of two gaussians (14.2% relative integrated area of the second gaussian) whose full-widths at half maximum (FWHM) were 6-7 ps and 22 ps for the first and the second gaussian respectively. Lifetimes associated with disconnected species were

expected to be the same for both excitation wavelengths and therefore linked during the sequential analysis.

The average decay time τ_{av} (Equation SI1-1) results from the sum of each lifetime weighted by the relative amplitudes of their DAS:

$$\tau_{av} = \sum_n(\tau_n \cdot A_n) / \sum_n A_n \quad \text{Equation SI1-1}$$

In Equation SI1-1, A_n is the area under the DAS of the n -th component. Only the components attributed to the PSI-LHCI-LHCII-related DAS are used in the calculation.

iii. Target analysis of the time-resolved measurements

On the basis of our PSI-LHCI kinetic model (Figure 3a, (17)), we used several constraints in the analysis of PSI-LHCI-LHCII (Figure 3b): we fixed the relative initial populations of the compartments associated to PSI-LHCI (Red, Bulk and Lhca2/a9) and the rate constants between Bulk and Lhca2/a9 given the limited information on Lhca2/a9 specifically in the two PSI-LHCI-LHCII datasets. Previous fitted Species Associated Spectra (SAS) of Red, Bulk and Lhca2/a9 (17) were used as additional information to guide the target analysis. The relative initial population of Lhcb (Table SI1-2) was fixed in the range as calculated above.

	Red	Bulk	Lhca2/a9	Lhcb
PSI-LHCI-LHCII upon 400 nm	5.8%	59.5%	6.7%	28.1%
PSI-LHCI-LHCII upon 475 nm	5.8%	44.8%	5.4%	44.0%

Table SI1-2: Relative initial populations of each compartment fixed during the target analysis.

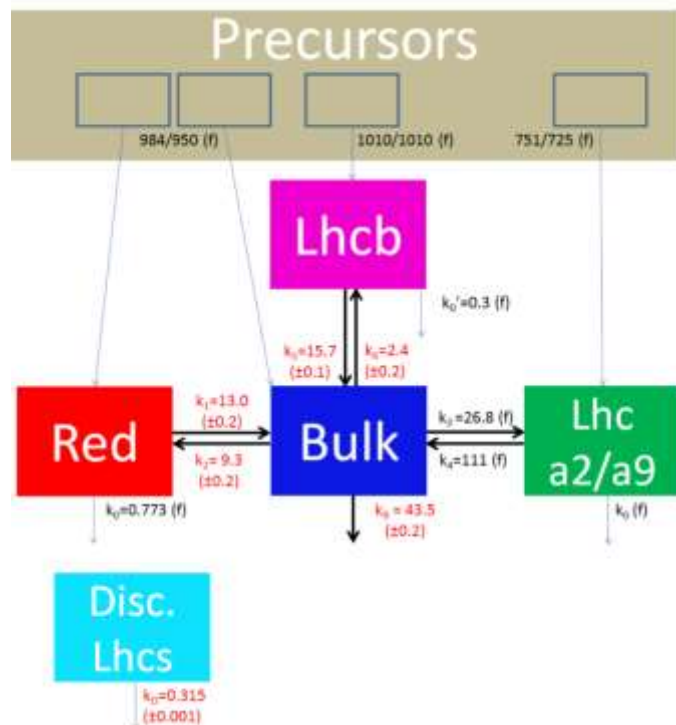
Using these constraints and assuming equal oscillator strength for each compartment species (equal area under the SAS, (18)), the forward and backward rate constants between Bulk and Lhcb as well as their SAS were fitted by means of a non-negative least-squares variable projection algorithm (14,15,19). The target analysis was performed on the two PSI-LHCI-LHCII datasets (upon 400 nm and 475 nm excitation) simultaneously. The IRF was modeled as a single gaussian (FWHM of 7-8 ps).

To compare its consistency with the sequential analysis, the average decay time from the target analysis was calculated by weighting the lifetimes (including the precursors lifetimes) by the corresponding overall amplitude of the trapping (last column in Table SI2-1). The overall amplitude of the trapping is obtained for each lifetime by summing all the amplitudes of the different compartments (Table 1 and Table SI2-1) with the amplitude of the precursors (Table SI1-2).

SI2: Results from the target analysis

i. Complete kinetic scheme

The complete kinetic model used for the target analysis is presented in Scheme SI2-1. The precursors contain emission from pigments transferring their energy faster (1-1.4 ps) than the time resolution of our instrument (~3 ps).



Scheme SI2-1: Complete kinetic model including precursors and compartments associated with the disconnected species (“Disc. Lhcs”, rate constant k_D). Rate constants are indicated in ns^{-1} , with uncertainties for the fitted rates (in red). Precursors depopulate at slightly different rate upon 400 nm and 475 nm excitation (left/right respectively) with relative amounts of depopulation indicated in Table SI1-2.

ii. Selection of time-resolved emission at 70 wavelengths

At all detection wavelengths, emission decay kinetics is captured by the kinetic model of PSI-LHCI-LHCII (Figure 4b) leading to a good overlap between the raw and the fitted traces (Figure SI2-1).

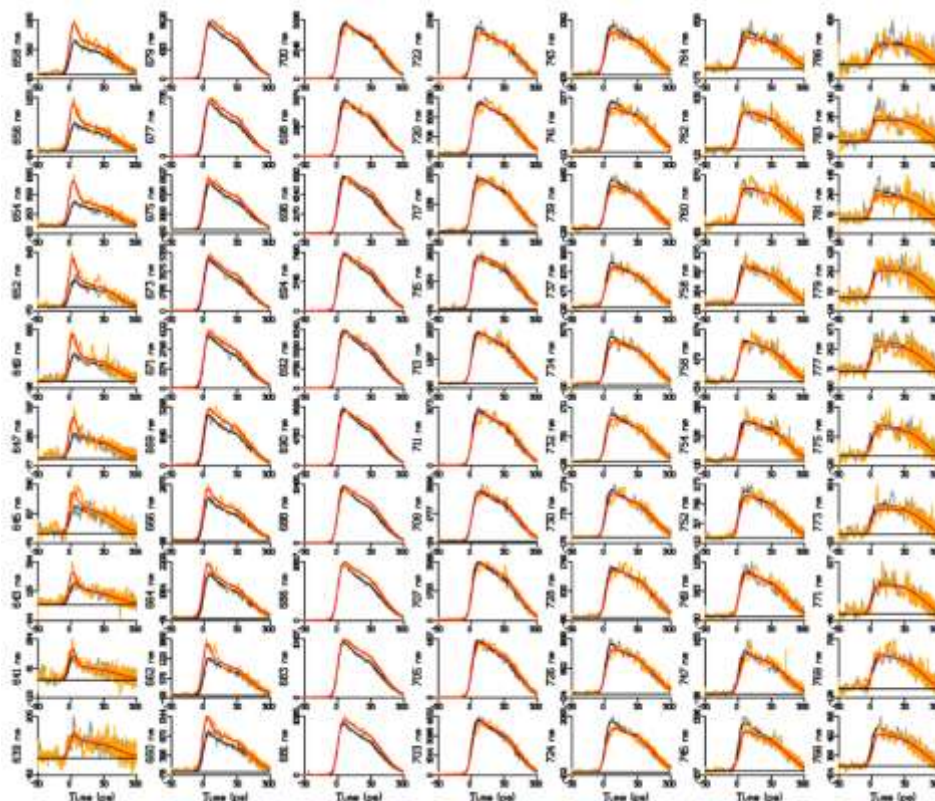


Figure SI2-1: Time-resolved emission (traces scaled to their maximum) at 70 wavelengths (indicated in the ordinate label) after excitation of PSI-LHCI-LHCII at 400 nm (grey) or 475 nm (orange). Black and red lines indicate the fit after target analysis.

iii. Comparison of Species Associated Spectra (SAS) of PSI-LHCI-related compartments. SAS of the precursors and the disconnected species

The PSI-LHCI compartments Red, Bulk and Lhca2/a9 do converge toward the previously calculated SAS ((17), Figure SI2-2a) as expected (see SI1-iii). The enthalpy of each compartment, approximated as the average spectral position of the SAS, is therefore similar in both particles.

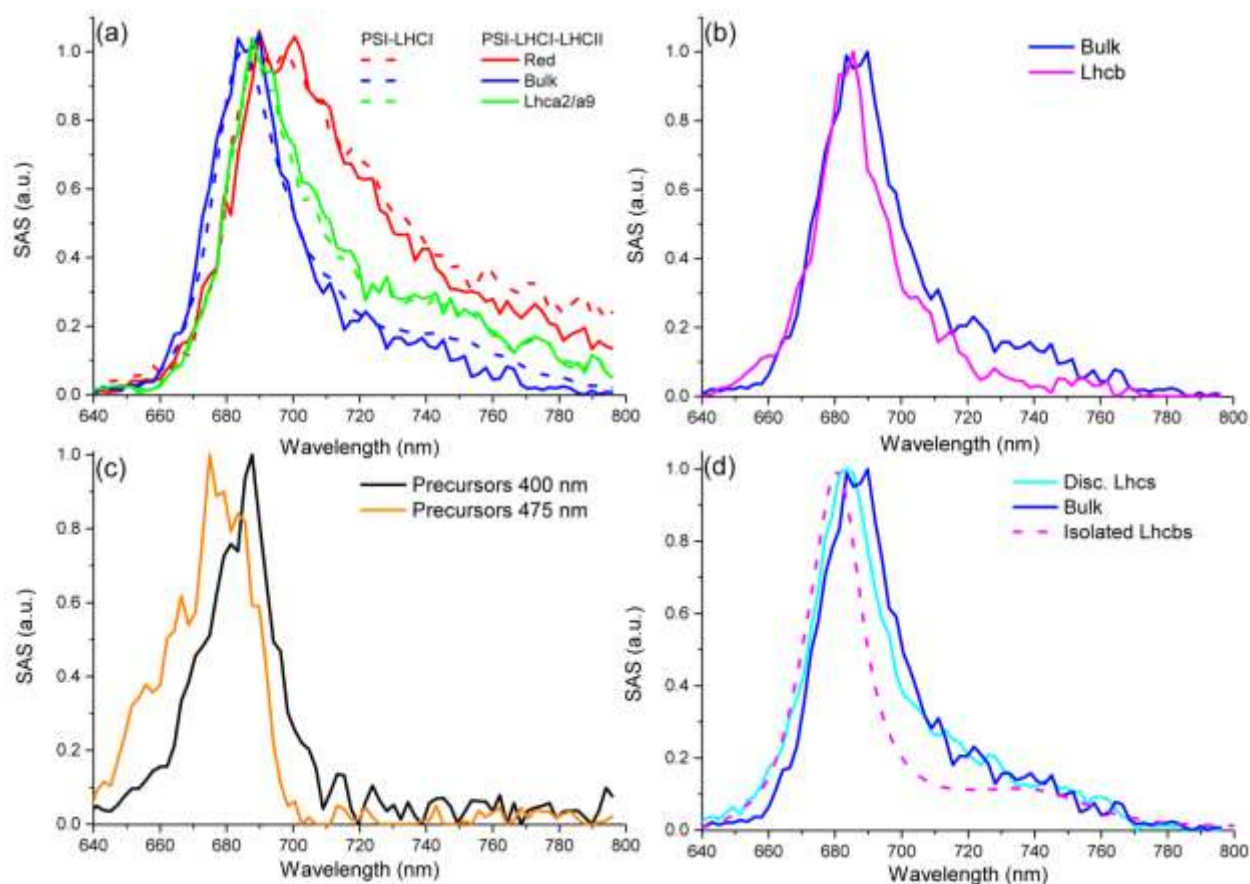


Figure SI2-2: SAS of: (a) Red, Bulk and Lhca2/a9 calculated from the target analysis of PSI-LHCI ((17), dashed) and from the target analysis of PSI-LHCI-LHCII (this study, solid); (b) Bulk and Lhcb, normalized to their maximum; (c) the precursors calculated from the target analysis of PSI-LHCI-LHCII, depending only on the excitation wavelength (400 nm or 475 nm); (d) Disconnected Lhcb compared to Bulk SAS and to the steady state emission spectrum of the isolated Lhcb.

The SAS of the precursors contain Chl *a* and Chl *b* emission, especially visible after 475 nm excitation for the latter (Figure SI2-2c). The SAS of the 3% disconnected species, Disc. Lhcs (Figure SI2-2d) overlap well on the blue edge with the emission of the isolated Lhcb, but also shows some additional amplitude in the red, which we attribute to the presence of Lhcas in this compartment.

iv. Estimation the number of Chls in PSI-LHCI-related compartments

The number of Chls in each compartment was obtained by a detailed balance analysis (see details of calculation in (17)).

From the target analysis of PSI-LHCI, it was previously estimated that 12 Chls were in Red, 163 in Bulk and 16 in Lhca2/a9 (17). Based on the recent crystal structure of PSI-LHCI (5), these estimations have to be adjusted. The total number of Chls in PSI-LHCI of higher plant revealed by this new crystal structure is 155, with 14 Chls per Lhca on average (5). This corresponds now to a total number of Chls *a* in *C. reinhardtii* PSI-LHCI of 183 (Table SI1-1) instead of 191 previously estimated (17). It leads to a new estimation of 11 Chls in Red, 156 in Bulk and 16 in Lhca2/a9.

From the target analysis of PSI-LHCI-LHCII, the equilibrium between Bulk and Red was a bit different compared to (17) (Figure 3) leading to a new estimation of the Chl number in the PSI-LHCI-related compartments. By use of the detailed balance (see details in (17)) and considering the enthalpy difference between the compartments unchanged compared to previous study ((17), Figure SI2-2a), 21

Chls were estimated in Red, 147 Chls in Bulk and 15 Chls in Lhca2/a9. In PSI-LHCI-LHCII, Red seems to contain more Chls than previously, telling that a small number of Chls previously in Bulk are now in faster equilibrium with the red Chls. The difference in Chls number in Bulk between the two studies can partly explain that the trapping rate is changing from $(29.2 \text{ ps})^{-1}$ in (17) to $(23.0 \text{ ps})^{-1}$ in the current work.

v. Amplitude matrices and concentration profiles

The lifetimes and their amplitude for each compartment are given in the amplitude matrices (Table 1 in main text upon 475 nm and Table SI2-1 upon 400nm).

PSI-LHCI-LHCII (400 nm excitation)					
Lifetimes	Red	Bulk	Lhca2/a9	Lhcb	Overall amplitude of the trapping
1.0 ps	0.000	0.005	0.000	-0.285	0.000
1.0 ps	-0.052	-0.651	0.020	0.002	-0.029
1.3 ps	0.000	0.013	-0.079	0.000	0.001
6.5 ps	-0.011	0.162	-0.103	-0.003	0.045
22.9 ps	-0.093	0.300	0.117	-0.026	0.299
63.8 ps	-0.200	0.042	0.012	0.258	0.111
97.3 ps	0.356	0.129	0.034	0.054	0.573

Table SI2-1: Amplitude matrices of PSI-LHCI-LHCII upon 400 nm and the overall amplitude of the trapping at each lifetime.

The time-dependence of the population of each compartment (concentration profile) is plotted in Figure SI2-3.

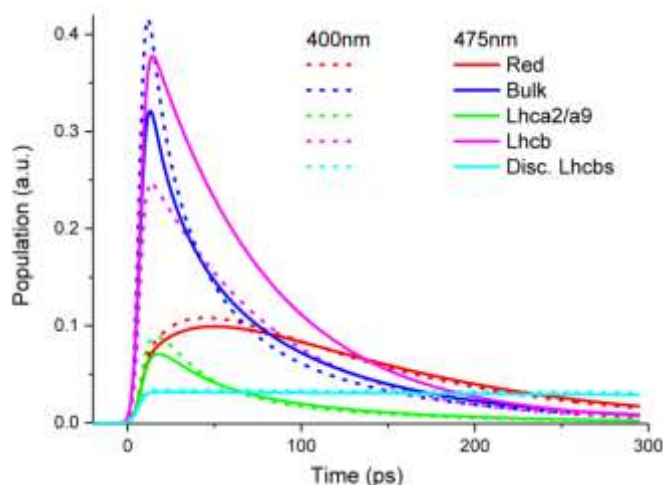


Figure SI2-3: Concentration profiles for each compartment obtained from the target analysis of PSI-LHCI-LHCII (Figure 3b) on the two datasets simultaneously (upon 400 nm, dashed curves, and 475 nm, solid curves).

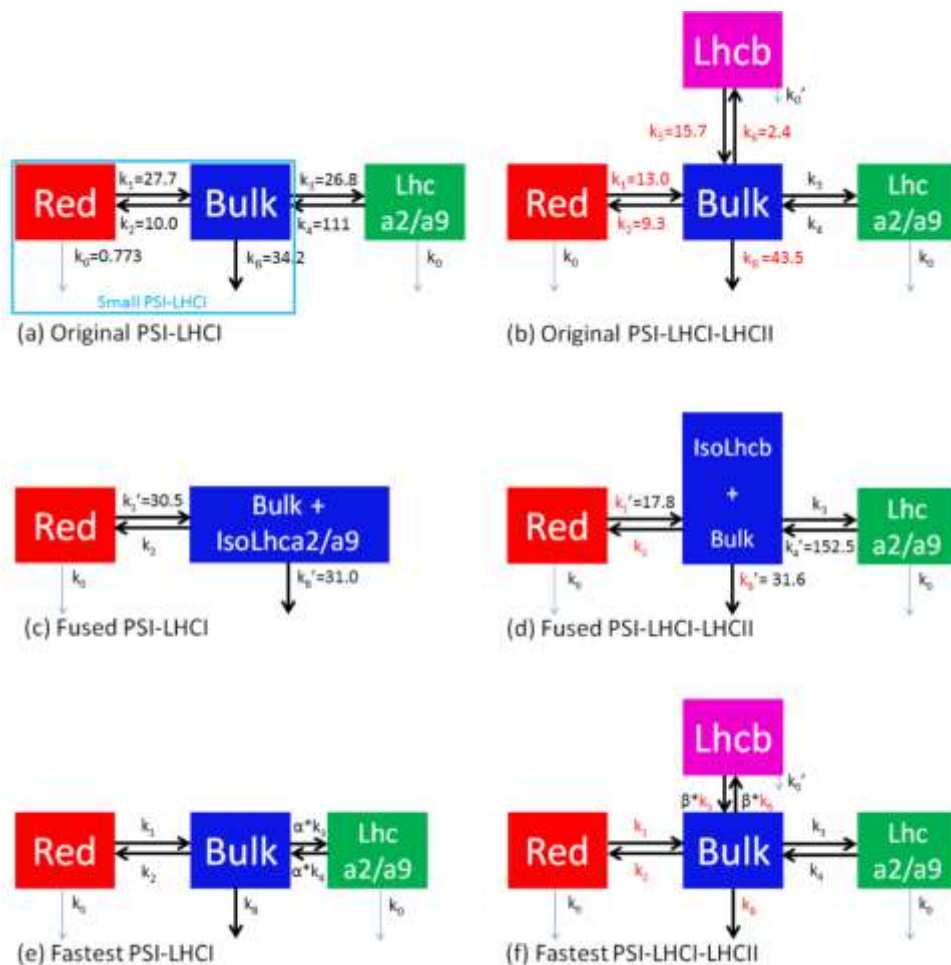
SI3: Quantifying the contributions of compartment size, composition and connectivity to the average decay time of PSI-LHCI and PSI-LHCI-LHCII

The addition of antennas can affect the average decay time in several ways depending on the free energy difference, ΔG , and on the connectivity between the antennas and the rest of the supercomplex. To independently study the effect of each factor, the decay kinetics of hypothetical PSI-LHCI and PSI-LHCI-

LHCII particles with altered compartment size and composition and/or connectivity (Scheme SI3-1) were simulated. The resulting average decay times, calculated from the amplitude matrices (in the same way as for the target analysis, see SI1-iii), are compared in Table SI3-1.

i. Change in compartment size and composition

The increase of antenna size when adding the Lhca2/a9 compartment to “Small PSI-LHCI” (Scheme SI3-1a) or the Lhcb compartment to the original PSI-LHCI (Scheme SI3-1a&b) was studied independently from their connectivity and their energy level by simulating “Fused PSI-LHCI” (Scheme SI3-1c) and “Fused PSI-LHCI-LHCII” (Scheme SI3-1d) respectively.



Scheme SI3-1: Simulated kinetic models of: (a) the original PSI-LHCI ((17) and Figure 3a). “Small PSI-LHCI” (light blue frame) corresponds to a particle composed of Red and Bulk compartments only (17); (b) the original PSI-LHCI-LHCII (Figure 3b). Rate constant indicated in black were fixed and those indicated in red were obtained from the target analysis (see Results); (c) In Fused PSI-LHCI, the Chls of Lhca2/a9 are assumed to be isoenergetic with Bulk (named “IsoLhca2/a9”) and these two compartments are fused (i.e. energy transfer infinitely fast); (d) Fused PSI-LHCI-LHCII where Chls of Lhcb are considered isoenergetic with Bulk (named “IsoLhcb”) and these two compartments are fused; (e) Fastest PSI-LHCI corresponding to PSI-LHCI where the connectivity between Bulk and Lhca2/a9 has been improved to its best (see below); (f) Fastest PSI-LHCI-LHCII corresponding to PSI-LHCI-LHCII where the connectivity between Bulk and Lhcb has been improved to its best (see below). The rate constants are in ns^{-1} .

Before changing the compartment size, we need to specify the compartments size in the original kinetic models (Figure 3). The target analysis of PSI-LHCI, gave 11 Chls in Red, 156 in Bulk and 16 in Lhca2/a9 (up-dated estimation of the Chl number, see SI2-iv). This estimation was used as initial values in the simulated models of PSI-LHCI (Scheme SI3-1c&e). The target analysis of PSI-LHCI-LHCII, gave 21 Chls in Red, 147 Chls in Bulk and 15 Chls in Lhca2/a9 (see SI2-iv). This estimation was used as initial values in the simulated models of PSI-LHCI-LHCII (Scheme SI3-1d&f).

In the “Fused PSI-LHCI” (Scheme SI3-1c), 16 Chls *a*, initially in Lhca2 and Lhca9, are now isoenergetic with Bulk Chls and perfectly coupled to them (IsoLhca2/a9). The change in Chls number in the fused compartment “Bulk+IsoLhca2/a9” modifies the trapping rate from this compartment to $k_B' = 31.0 \text{ ns}^{-1}$ (intrinsic charge separation rate multiplied by the number of Chls contained in the compartment = $34.2 \text{ ns}^{-1} * 156 / (156 + 16)$). When considering the spectral overlap between the fused “Bulk+IsoLhca2/a9” compartment and Red, we must picture the absorption spectrum of “Bulk+IsoLhca2/a9” as the absorption of Bulk increased proportionally by the additional Chls contained in Lhca2/a9 whereas “Bulk+IsoLhca2/a9” emission spectrum stays unchanged compared to Bulk given that the area under the spectrum is normalized to 1 on the frequency scale (see details in SI3-iii and Figure SI3-1). As the spectral overlap changes only when the fused compartment is the acceptor, only k_1 , the backward EET rate to “Bulk+IsoLhca2/a9”, is affected (Equations SI3-3 and SI3-4) and increases to k_1' , the other rate k_2 been unchanged (Scheme SI3-1c).

In “Fused PSI-LHCI-LHCII” (Scheme SI3-1d), 55 Chls, which in the model of Figure 3b are in the “Lhcb” compartment, are now isoenergetic with Bulk Chls and perfectly coupled to them (IsoLhcb). The trapping rate from the fused compartment “Bulk+IsoLhcb” changes to $k_B' = 31.6 \text{ ns}^{-1}$ ($43.5 \text{ ns}^{-1} * 147 / (147 + 55)$). The backward EET rates to Bulk+IsoLhcb, k_1 and k_4 , increase to k_1' and k_4' , the other rates k_2 and k_3 been unchanged.

The initial population in the fused compartment corresponds to the sum of the initial populations of the two separated compartments.

ii. Change in compartment connectivity

Qualitatively, an increased connectivity between compartments can be interpreted as a decreased distance between them. In the frame of the Förster theory (Equation SI3-1), if *R* is reduced by a positive factor $\sqrt[6]{\alpha}$, the forward and backward rates will both increase by a factor “ α ”, speeding up the equilibrium between donor and acceptor. Similar conclusion can be drawn in the limit of strong coupling since $k_{EET} \propto \frac{1}{R^x}$, where *x* depends on the theoretical framework.

From the original kinetic model of PSI-LHCI (Scheme SI3-1a), the connectivity was improved by multiplying the forward and backward rates between Bulk and Lhca2/a9 in “Fastest PSI-LHCI” by different values of α (Scheme SI3-1e). At increasing α , the average decay time of PSI-LHCI decreases to a minimum. From the kinetic model of PSI-LHCI-LHCII (Scheme SI3-1b), the connectivity was improved by multiplying the forward and backward rates between Bulk and Lhcb in “Fastest PSI-LHCI-LHCII” by different values of β (Scheme SI3-1f). At increasing β , the average decay time of PSI-LHCI-LHCII decreases to a minimum.

The final “optimum” values of α or β were chosen such that the resulting average decay time was 1 ps above the value for α or β infinite.

iii. Detailed calculation of rate constants when changing compartments size

The changes in compartments size and connectivity are pictured here in the frame of the Förster theory but qualitatively similar conclusions could be drawn when using other approximations. The Förster theory describes weak excitonic interactions between a donor (D) that transfers its energy to an acceptor (A) with EET rate k_{DA} described by the Förster equation (20,21):

$$k_{DA} = \frac{\kappa^2}{\tau_D} \cdot \left(\frac{R_0}{R}\right)^6 \quad \text{Equation SI3-1}$$

where R is the distance between the donor and the acceptor, τ_R^D the intrinsic radiative lifetime of the donor, κ the dimensionless orientation factor between the donor and acceptor transition dipole moments and R_0 the Förster radius that increases with the spectral overlap integral $J(\nu)$

$$J(\nu) = \int_0^\infty \frac{\varepsilon_A(\nu) F_D(\nu)}{\nu^4} d\nu \text{ Equation SI3-2}$$

where $\varepsilon_A(\nu)$ the molar extinction coefficient of the acceptor and $F_D(\nu)$ the fluorescence emission of the donor, normalized to 1 when integrated on the frequency scale ν .

The extinction coefficient of the acceptor compartment ($\varepsilon_A(\nu)$ in Equation SI3-2) depends on the number of Chls in this compartment whereas the emission of the donor compartment is normalized to 1 in the spectral overlap integral ($F_D(\nu)$ in Equation SI3-2) and will not vary if the donor compartment changes size. The fused compartments (Bulk+IsoLhca2/a9 and Bulk+IsoLhcb) have their absorption spectra proportionally increased compared to the spectrum of Bulk according to their Chls number whereas they have the same emission spectra as Bulk (Figure SI3-1). The overlap integral between compartments, and therefore the EET rate, is affected only when the fused compartments are acceptors. Therefore, k_1 in PSI-LHCI increases to k_1' in Fused PSI-LHCI (Scheme SI3-1c) and k_1 and k_4 in PSI-LHCI-LHCII increase to k_1' and k_4' in Fused-PSI-LHCI-LHCII (Scheme SI3-1d). By contrast, all the other rates are unchanged.

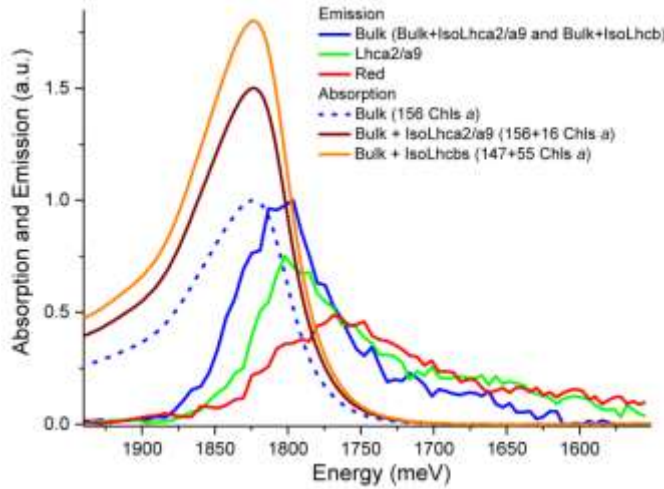


Figure SI3-1: Absorption and emission spectra of Bulk (with changing size) and emission spectra of Red (red) and Lhca2/a9 (green). The absorption of Bulk with 156 Chls a (dashed blue) is approximated as the normalized absorption of Small PSI-LHCI (blue frame in Scheme SI3-1a). The absorption of Bulk+IsoLhca2/a9 with 156+16 Chls a (solid Brown) and of Bulk+IsoLhcb with 147+55 Chls a (solid Orange) increase proportionally with the Chls number. The fluorescence emission spectra of the fused compartments Bulk+IsoLhca2/a9 and Bulk+IsoLhcb are the same as Bulk (solid blue).

To quantify the new rate constants, we used a detailed balance: the free energy difference ΔG between two compartments i and j can be calculated from the forward and backward rate constants: $\Delta G_{ij} = G_j - G_i = -k_B T \cdot \ln(k_{i \rightarrow j}/k_{j \rightarrow i})$. With the free energy expressed in function of the enthalpy H and the entropy S , $\Delta G_{ij} = \Delta H_{ij} - T\Delta S_{ij}$, and the entropy difference expressed in function of the number of Chls N_i and N_j in compartments i and j , $\Delta S_{ij} = -k_B \cdot \ln(N_i/N_j)$, we can write the detailed balance:

$$\frac{k_{i \rightarrow j}}{k_{j \rightarrow i}} = \frac{N_j}{N_i} * \exp\left(\frac{-(H_j - H_i)}{k_B T}\right) \text{ Equation SI3-3}$$

For instance in the case of Fused PSI-LHCI (Scheme SI3-1c), considering that k_2 stays unchanged (see above), k_1' is calculated as:

$$k_1' = k_2 * \frac{N_{(\text{Bulk+Iso-Lhca2/a9})}}{N_{\text{Red}}} * \exp\left(\frac{-(H_{(\text{Bulk+Iso-Lhca2/a9})} - H_{\text{Red}})}{k_B T}\right) \text{ Equation SI3-4}$$

With the same approach, k_1' and k_4' were calculated.

iv. Results from the simulated kinetics

The effect of antenna size enlargement due to the addition of Lhca2 and Lhca9 to PSI can be studied independently from the connectivity and energy of these two subunits by simulating the hypothetical “Fused PSI-LHCI particle” (Scheme SI3-1c) where Bulk has been enlarged by the same number of Chls that are present in Lhca2 and Lhca9. Fused PSI-LHCI has an average decay time of 45.7 ps upon 400 nm excitation and 46.5 ps upon 475 nm excitation (Table SI3-1). The effect of the antenna enlargement due to the addition of two Lhcas is quantified by subtracting the average decay times of PSI-LHCI in the absence of Lhca2 and Lhca9 (Small PSI-LHCI, blue frame in Scheme SI3-1a) to that of Fused PSI-LHCI and it corresponds to a difference of 2.5 ps at 400 nm and 2.3 ps at 475 nm.

PSI-LHCI		
	400 nm	475 nm
Original	50.5	51.4
Small PSI-LHCI	43.2	44.2
Fused	45.7	46.5
Fastest (“optimum” $\alpha=1$)	50.5	51.4
PSI-LHCI-LHCII		
	400 nm	475 nm
Original	69.7	79.4
PSI-LHCI-related compartments	50.8	52.6
Fused	56.5	56.5
Fastest (“optimum” $\beta=18$)	53.6	54.1

Table SI3-1: Average decay time from the original and the simulated kinetic models of PSI-LHCI and PSI-LHCI-LHCII particles with modified compartments connectivity, size and composition (Scheme SI3-1).

To study the connectivity of the Lhca2/a9 compartment with PSI-LHCI, we simulate the hypothetical “Fastest PSI-LHCI” (Scheme SI3-1e) where the connectivity was improved to obtain the fastest possible average decay time of the particle (see SI3-ii). The average decay time of PSI-LHCI remains always the same (“optimum” $\alpha=1$), leading to the conclusion that the connectivity between Bulk and Lhca2/a9 is very high in the original PSI-LHCI although Lhca2 and Lhca9 are the first complexes to be lost after detergent treatment of PSI-LHCI (6). Based on these results, we can then conclude that the difference between PSI-LHCI and Fused PSI-LHCI is due to the presence of red Chls in Lhca2/a9 that slow down the kinetics by 4.8 ps at 400 nm and 4.9 ps at 475 nm.

In a similar way we investigate the influence of the Lhcbs to the PSI-LHCI-LHCII average decay time in terms of connectivity, size and composition. The effect of the increase in the antenna size of PSI-LHCI by adding Lhcbs can be obtained by simulating the hypothetical particle “Fused PSI-LHCI-LHCII” (Scheme SI3-1d). Fused PSI-LHCI-LHCII has an average decay time of 56.5 ps for both excitation wavelengths (Table SI3-1), longer than in the absence of Lhcbs by 5.7 ps upon 400 nm and 3.9 ps upon 475 nm (subtraction of Fused PSI-LHCI-LHCII and a particle made of PSI-LHCI-related compartments only). By improving the original connectivity between Bulk and Lhcb, the “Fastest PSI-LHCI-LHCII” (Scheme SI3-1f) is obtained after multiplying the forward and backward rate constants between these two compartments by an “optimum” $\beta=18$ and corresponds to a fastest average decay times of 53.6 ps upon

400 nm and 54.1 ps upon 475 nm (Table SI3-1), 16.1 ps and 25.3 ps faster than the original PSI-LHCI-LHCII average decay times upon 400 nm and 475 nm respectively. The higher energy of Lhcbs compared to the bulk is favoring the forward transfer to the bulk and partially counteracts the negative effect of the connectivity. We can directly estimate the influence of the presence of blue Chls in Lhcb by looking at the difference between Fused PSI-LHCI-LHCII and Fastest PSI-LHCI-LHCII, since the connectivity is very high in both particles. The bluer Chls of Lhcbs decreases the average decay time of PSI-LHCI-LHCII by 2.9 ps at 400nm and 2.4 ps at 475 nm.

REFERENCES FOR SUPPLEMENTAL DATA

1. Sauer, K., Smith, J. R. L., and Schultz, A. J. (1966) The Dimerization of Chlorophyll a, Chlorophyll b, and Bacteriochlorophyll in Solution1. *J. Am. Chem. Soc.* **88**, 2681-2688
2. Croce, R., Canino, G., Ros, F., and Bassi, R. (2002) Chromophore organization in the higher-plant photosystem II antenna protein CP26. *Biochemistry* **41**, 7334-7343
3. de Weerd, F. L., Kennis, J. T., Dekker, J. P., and van Grondelle, R. (2003) β -Carotene to Chlorophyll Singlet Energy Transfer in the Photosystem I Core of *Synechococcus elongatus* Proceeds via the β -Carotene S2 and S1 States. *J. Phys. Chem. B* **107**, 5995-6002
4. Wientjes, E., van Stokkum, I. H. M., van Amerongen, H., and Croce, R. (2011) The role of the individual Lhcas in photosystem I excitation energy trapping. *Biophys. J.* **101**, 745-754
5. Qin, X., Suga, M., Kuang, T., and Shen, J.-R. (2015) Structural basis for energy transfer pathways in the plant PSI-LHCI supercomplex. *Science* **348**, 989-995
6. Drop, B., Webber-Birungi, M., Fusetti, F., Kouril, R., Redding, K. E., Boekema, E. J., and Croce, R. (2011) Photosystem I of *Chlamydomonas reinhardtii* contains nine light-harvesting complexes (Lhca) located on one side of the core. *J. Biol. Chem.* **286**, 44878-44887
7. Mazor, Y., Borovikova, A., and Nelson, N. (2015) The structure of plant photosystem I super-complex at 2.8 Å resolution. *Elife* **4**
8. Drop, B., Yadav K.N, S., Boekema, E. J., and Croce, R. (2014) Consequences of state transitions on the structural and functional organization of Photosystem I in the green alga *Chlamydomonas reinhardtii*. *Plant J.* **78**, 181-191
9. Pan, X., Liu, Z., Li, M., and Chang, W. (2013) Architecture and function of plant light-harvesting complexes II. *Curr. Opin. Struct. Biol.* **23**, 515-525
10. Liu, Z., Yan, H., Wang, K., Kuang, T., Zhang, J., Gui, L., An, X., and Chang, W. (2004) Crystal structure of spinach major light-harvesting complex at 2.72 Å resolution. *Nature* **428**, 287-292
11. Wientjes, E., Oostergetel, G. T., Jansson, S., Boekema, E. J., and Croce, R. (2009) The role of Lhca complexes in the supramolecular organization of higher plant photosystem I. *J. Biol. Chem.* **284**, 7803-7810
12. Drop, B., Webber-Birungi, M., Yadav, S. K. N., Filipowicz-Szymanska, A., Fusetti, F., Boekema, E. J., and Croce, R. (2014) Light-harvesting complex II (LHCII) and its supramolecular organization in *Chlamydomonas reinhardtii*. *Biochim. Biophys. Acta* **1837**, 63-72
13. Snellenburg, J. J., Laptinok, S., Seger, R., Mullen, K. M., and Van Stokkum, I. H. (2012) Glotaran: A Java-based graphical user interface for the R package TIMP. *Journal of statistical software* **49**
14. van Stokkum, I. H. M., Larsen, D. S., and van Grondelle, R. (2004) Global and target analysis of time-resolved spectra. *Biochim. Biophys. Acta* **1657**, 82-104
15. van Stokkum, I. H. M., Larsen, D. S., and van Grondelle, R. (2004) Erratum to “Global and target analysis of time-resolved spectra”[*Biochimica et Biophysica Acta* 1658/2–3 (2004) 82–104]. *Biochim. Biophys. Acta* **1658**, 262
16. van Stokkum, I. H. M., van Oort, B., van Mourik, F., Gobets, B., and van Amerongen, H. (2008) (Sub)-picosecond spectral evolution of fluorescence studied with a synchroscan streak-camera system and target analysis. in *Biophysical techniques in photosynthesis*, Springer. pp 223-240

17. Le Quiniou, C., Tian, L., Drop, B., Wientjes, E., van Stokkum, I. H. M., van Oort, B., and Croce, R. (2015) PSI-LHCI of *Chlamydomonas reinhardtii*: Increasing the absorption cross section without losing efficiency. *Biochim. Biophys. Acta* **1847**, 458-467
18. Snellenburg, J. J., Dekker, J. P., van Grondelle, R., and van Stokkum, I. H. M. (2013) Functional compartmental modeling of the photosystems in the thylakoid membrane at 77 K. *J. Phys. Chem. B* **117**, 11363-11371
19. Mullen, K. M., and Van Stokkum, I. H. M. (2009) The variable projection algorithm in time-resolved spectroscopy, microscopy and mass spectrometry applications. *Numerical Algorithms* **51**, 319-340
20. Förster, T. (1946) Energiewanderung und Fluoreszenz. *Naturwissenschaften* **33**, 166-175
21. Förster, T. (1948) Zwischenmolekulare Energiewanderung und Fluoreszenz. *Annalen der Physik* **437**, 55-75

The High Efficiency of Photosystem I in the Green Alga *Chlamydomonas reinhardtii* Is Maintained after the Antenna Size Is Substantially Increased by the Association of Light-harvesting Complexes II

Clotilde Le Quiniou, Bart van Oort, Bartłomiej Drop, Ivo H. M. van Stokkum and Roberta Croce

J. Biol. Chem. 2015, 290:30587-30595.

doi: 10.1074/jbc.M115.687970 originally published online October 26, 2015

Access the most updated version of this article at doi: [10.1074/jbc.M115.687970](https://doi.org/10.1074/jbc.M115.687970)

Alerts:

- [When this article is cited](#)
- [When a correction for this article is posted](#)

[Click here](#) to choose from all of JBC's e-mail alerts

Supplemental material:

<http://www.jbc.org/content/suppl/2015/10/26/M115.687970.DC1.html>

This article cites 51 references, 15 of which can be accessed free at <http://www.jbc.org/content/290/51/30587.full.html#ref-list-1>